Extended dilation of the radiocarbon time scale between 40,000 and 48,000 y BP and the overlap between Neanderthals and *Homo sapiens*

Edouard Bard[a,1], Timothy J. Heaton[b], Sahra Talamo[c], Bernd Kromer[d], Ron W. Reimer[e], and Paula J. Reimer[e]

[a]CEREGE, Aix-Marseille University, CNRS, IRD, INRAE, Collège de France, Technopôle de l'Arbois, 13545 Aix-en-Provence, France; [b]School of Mathematics and Statistics, University of Sheffield, S3 7RH Sheffield, United Kingdom; [c]Department of Chemistry G. Ciamician, Alma Mater Studiorum, University of Bologna, 40126 Bologna, Italy; [d]Institute of Environmental Physics, Heidelberg University, 69120 Heidelberg, Germany; and [e]The ^{14}CHRONO Centre for Climate, the Environment and Chronology, School of Natural and Built Environment, Queen's University Belfast, BT7 1NN Belfast, United Kingdom

Edited by Thure E. Cerling, University of Utah, Salt Lake City, UT, and approved July 14, 2020 (received for review June 19, 2020)

The new radiocarbon calibration curve (IntCal20) allows us to calculate the gradient of the relationship between ^{14}C age and calendar age over the past 55 millennia before the present (55 ka BP). The new gradient curve exhibits a prolonged and prominent maximum between 48 and 40 ka BP during which the radiocarbon clock runs almost twice as fast as it should. This radiocarbon time dilation is due to the increase in the atmospheric ^{14}C/^{12}C ratio caused by the ^{14}C production rise linked to the transition into the Laschamp geomagnetic excursion centered around 41 ka BP. The major maximum in the gradient from 48 to 40 ka BP is a new feature of the IntCal20 calibration curve, with far-reaching impacts for scientific communities, such as prehistory and paleoclimatology, relying on accurate ages in this time range. To illustrate, we consider the duration of the overlap between Neanderthals and *Homo sapiens* in Eurasia.

radiocarbon | geochronology | paleomagnetism | Neanderthal

The radiocarbon method is the most widely used dating method over the past 55 ka BP. It relies on the beta decay of the ^{14}C isotope produced in the upper atmosphere by interaction with cosmic-ray particles. Samples of organic material or carbonates dated by ^{14}C either incorporated their carbon directly from the atmosphere as in plant photosynthesis, indirectly through the food chain, or by various chemical reactions. The ^{14}C content of a fossil sample is compared to the atmospheric ^{14}C content, which constitutes the starting reference for its disappearance by radioactive decay with a half-life of 5,700 ± 30 y.

In its raw form, the ^{14}C method is not accurate as atmospheric ^{14}C content has not been constant over time, instead having varied due to changes in its production rate and global carbon cycle rearrangements. To calculate a true calendar age from a ^{14}C measurement, one needs to know the initial atmospheric ^{14}C/^{12}C ratio at the time the sample carbon last exchanged with the atmosphere. We therefore calibrate the radiocarbon method by comparing ^{14}C measurements against samples for which accurate ("true") ages have been measured with independent dating techniques such as counting tree rings in subfossil tree logs, counting annually laminated sediments, or dating corals and stalagmites using uranium–thorium (U-Th). Over the past three decades, the resulting radiocarbon calibration curves have been provided by an international working group (IntCal). The new IntCal20 curve covering the past 55 ka BP has just been published (1), updating the previous IntCal13 version (2).

Over the past 55 ka, the ^{14}C calibration curve shows that ^{14}C ages are usually younger than true ages (1, 2), that is, the ^{14}C clock generally ticks at a slower pace than it should. This is due to the overall decrease of the atmospheric ^{14}C/^{12}C ratio over the past 40 ka (Fig. 1*D*), which partly compensates for the loss by radioactive decay in dated samples. Additionally, the relationship between ^{14}C ages and true calendar ages is far from linear. Compression of the ^{14}C time scale is particularly obvious during specific periods called ^{14}C age plateaus, when the decreasing atmospheric ^{14}C/^{12}C ratio fully compensates for radioactive decay. This implies that archeological sites and artifacts from these periods cannot be dated precisely with radiocarbon. The ^{14}C age plateaus on the order of a few centuries are linked to modulation of cosmogenic production by variable solar activity. Longer age plateaus may correspond to changes in the carbon cycle and deep ocean circulation, for example during the plateau that occurred at the end of the Younger Dryas climatic event (3–5).

In parallel to periods when the ^{14}C clock runs too slowly, there are also specific periods characterized by an increasing atmospheric ^{14}C/^{12}C ratio—also a consequence of solar and carbon cycle changes. Here, the ^{14}C clock ticks faster than it should.

One major outcome of the recent IntCal20 curve is that the pace of the ^{14}C clock can be calculated at unprecedented precision. We have computed the evolution of the first derivative of the IntCal20 curve, focusing on its multimillennial component (Fig. 1*A*). Over most of the past 55 ka, the gradient is below 1, meaning that the ^{14}C time scale is mostly compressed. However, the gradient is also characterized by a prominent maximum from 48 to 40 ka BP, reaching values up to 1.5 to 2 for the different sliding windows. Over this multimillennial period, there are about twice as many ^{14}C years as calendar years.

This expanded ^{14}C time scale was absent, or much less prominent, in former calibration curves, as seen by the comparison with IntCal13 (Fig. 1*A*). The 48 to 40 ka BP gradient maximum is directly tied to the rising trend of atmospheric Δ^{14}C, minimal until 48 ka BP before rising by more than 500‰ over a period of only a few millennia, to reach a maximum around 40 ka BP. As shown, the Δ^{14}C maximum (Fig. 1*D*) is broadly in phase with the minimum intensity of the geomagnetic field (Fig. 1*B*) during the Laschamp excursion (6) and the maximum concentration of ^{10}Be (Fig. 1*C*) measured in polar ice (7)—^{10}Be is also formed by cosmic-ray particles. The precise relationships, in phase and amplitude, between ^{14}C, ^{10}Be, and paleomagnetic intensity are complex, notably because ^{14}C atoms are mixed in the global carbon cycle, but can be studied with numerical models (7–10).

The maximum Δ^{14}C value above modern, ~700‰ at 41 ka BP, has been known from ^{14}C and U-Th dating in corals since the late 1990s (8), but the earlier Δ^{14}C minimum around 50 to 45 ka BP was only evidenced later with marine sediments (9, 11). The Δ^{14}C record prior to 40 ka BP has been refined with independent data

Author contributions: E.B. designed research; E.B., T.J.H., and S.T. performed research; E.B., T.J.H., S.T., B.K., R.W.R., and P.J.R. analyzed data; and E.B. wrote the paper.

The authors declare no competing interest.

[1]To whom correspondence may be addressed. Email: bard@cerege.fr.

This article contains supporting information online at https://www.pnas.org/lookup/suppl/doi:10.1073/pnas.2012307117/-/DCSupplemental.

First published August 17, 2020.

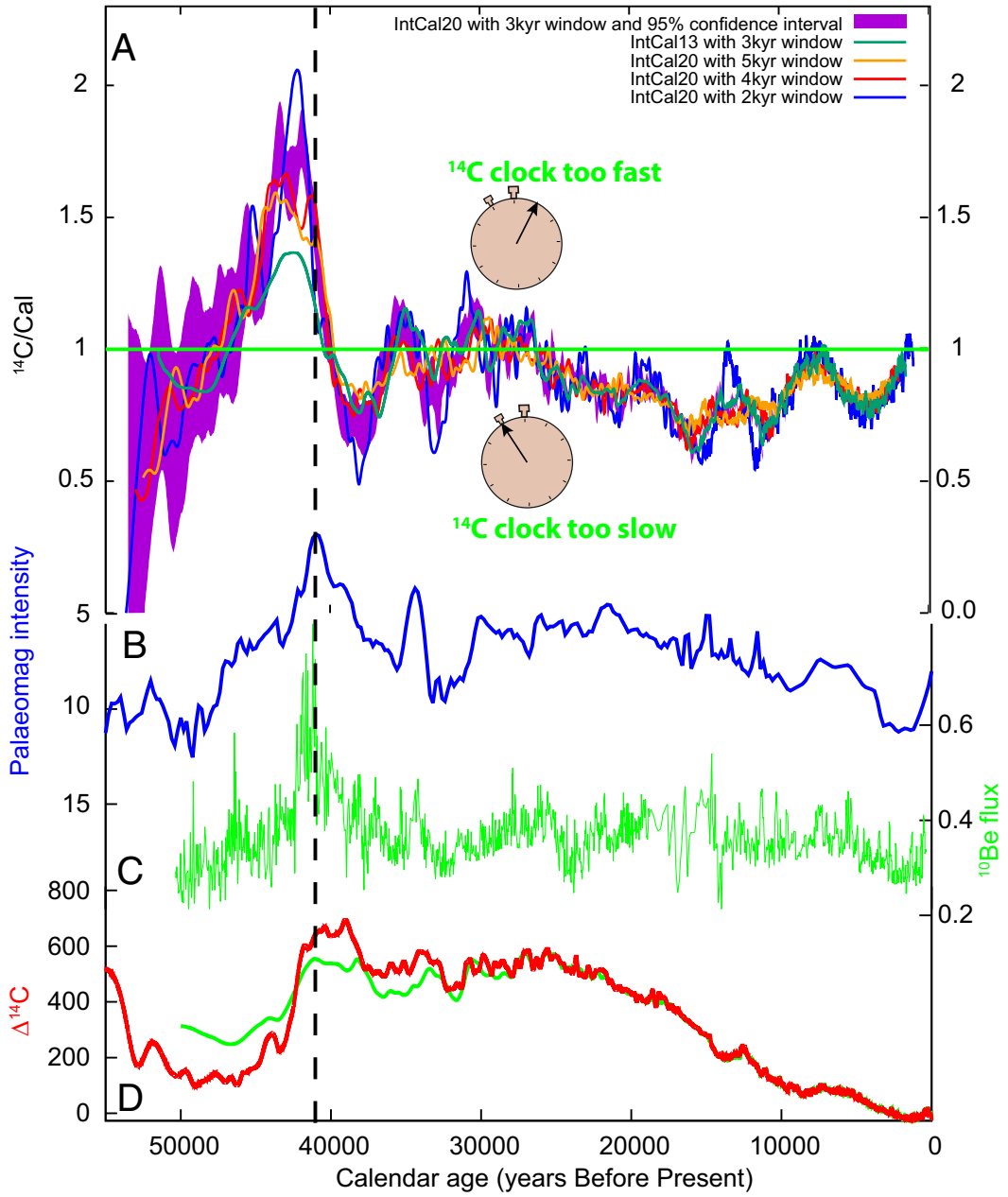

Fig. 1. (*A*) First derivative of the IntCal20 curve (1) computed by calculating the ^{14}C age vs. calendar age gradient over sliding windows of between 5,000- and 2,000-y durations. The purple area shows the 95% confidence interval for the 3,000-y window (to maintain legibility this is the only interval plotted). The green curve shows the first derivative of the IntCal13 curve (2) using the 3,000-y window (to be compared with the purple curve for IntCal20). When the gradient is above (below) unity, the ^{14}C clock ticks faster (slower) than it should. (*B*) Evolution of the intensity (in 10^{22}Am^2) of the geomagnetic field (6); note the reversed scale. (*C*) The ^{10}Be flux (in 10^6 atoms·cm^{-2}·y^{-1}) measured in Greenland ice cores (7). (*D*) Atmospheric Δ^{14}C (in per mille above modern) based on the IntCal20 in red (1) and IntCal13 in green (2). The prominent maximum of the gradient curve (*A*) centered around 43 ka BP corresponds to the rising phase of the Δ^{14}C curve (*D*) and thus predates the Δ^{14}C and ^{10}Be flux maxima (*C*) and the paleomagnetic intensity minimum (*B*) corresponding to the Laschamp geomagnetic excursion (vertical dashed line).

based on counting tree rings in subfossil kauri logs from New Zealand (12), and with ^{14}C and U-Th dating of stalagmites from the Hulu Cave in China (10). These independent data and their updates confirmed each other and were used collectively with updated statistical techniques (13) in order to construct the new IntCal20 calibration curve (1).

The radiocarbon time dilation over the 48 to 40 ka BP window, occurring just before the Δ^{14}C maximum, is thus a novel and major feature of the new IntCal20 curve. This time expansion effect has remained unnoticed, even though it was present to a lower extent in IntCal13. The difference between IntCa20 and IntCal13 is mainly linked to new data, notably Hulu stalagmites (10) and kauri trees (12), corrections and screening of existing data (1), and improved statistical modeling (13).

To illustrate the impact of the 48- to 40-ka-BP time dilation, Fig. 2 presents the ^{14}C and calendar chronologies of a selection of prehistoric sites dated using ^{14}C from human bone collagen. This includes famous sites occupied by Neanderthals (in red) and by *Homo sapiens* (in blue). In terms of the radiocarbon clock, the chronological overlap between the oldest *H. sapiens* remains

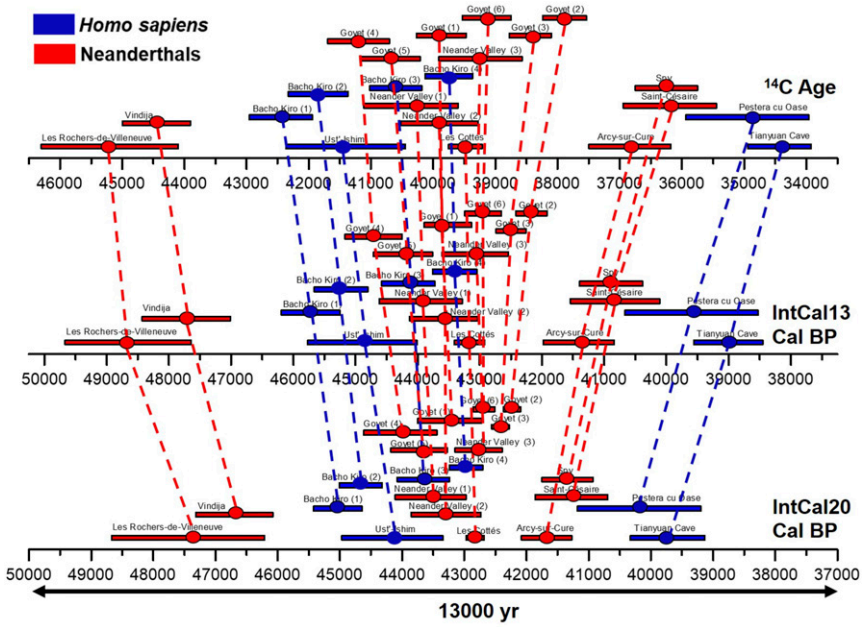

Fig. 2. Comparison between radiocarbon ages (*Upper*) and corresponding calibrated ages with IntCal13 (*Middle*) and IntCal20 (*Lower*) for a selection of human bone samples of Neanderthals (red) and early *H. sapiens* (blue). The ^{14}C ages ($\pm 1\sigma$) were calibrated using IntCal13 (ref. 2, *Middle*) and IntCal20 (ref. 1, *Lower*) in OxCal 4.2 (16). Note that the time axes of the three panels have exactly the same duration (13,000 y). The oblique dashed lines highlight the time dilation effect centered around 43 ka BP. Dataset S1 provides data and sources.

(Bacho Kiro Cave) and the youngest Neanderthal age (Saint-Césaire) is 6,250 ± 910 ^{14}C years (uncalibrated). When calibrated against the IntCal13 and IntCal20 curves, this difference is reduced to 5,000 ± 860 and 3,960 ± 710 calendar years, respectively, clearly illustrating how the expanded ^{14}C time scale is compressed by about 60% after conversion to calendar ages with the new IntCal20 calibration. We note, however, that to investigate possible cultural and genetic exchanges, contact between two populations should be considered at a regional scale for adjacent sites.

For prehistory and human evolution, the impact of the 48 to 40 ka BP time dilation goes beyond the study of late Neanderthal and early *H. sapiens* in Europe. Indeed, it will also affect the current discussion on *H. sapiens* spread across Eurasia and into Australia and help improve the genetic clock with a better calibration of genome mutation rates (e.g., refs. 14 and 15).

The new prominent maximum between 48 and 40 ka BP in the gradient between ^{14}C and calendar years is important as it enables improved resolution to separate events during this period (e.g., different stratigraphic levels in the same site). In addition to the compression converting ^{14}C to calendar time, the combined effects of the radiocarbon time dilation and the IntCal data improvements also lead to increased calendar age precision (e.g., the 1σ uncertainty for the Les Cottés Neanderthal in Fig. 2 ranges from 270 in ^{14}C years to 250 and 160 calendar years with IntCal13 and IntCal20, respectively). Determining the relative calendar age ordering of multiple events dated by ^{14}C in this period is therefore not affected. The structure of IntCal20 beyond 40 ka BP reinforces the need to measure accurately and precisely the small ^{14}C content of old samples, and in particular the use of updated pretreatment techniques to purify the original carbon fraction in order to eliminate residual contaminations.

Data Availability. All study data are included in the paper and Dataset S1.

ACKNOWLEDGMENTS. E.B. is supported by the EQUIPEX ASTER-CEREGE, the Collège de France, and the Agence Nationale de la Recherche project CARBOTRYDH. P.J.R. acknowledges the support of the UK Research and Innovation Natural Environment Research Council (Grant NE/M004619/1). T.J.H. is supported by Leverhulme Trust Fellowship RF-2019-140\9. We thank both referees for their useful comments.

1. P. J. Reimer *et al.*, The IntCal20 Northern Hemisphere radiocarbon calibration curve (0-55 kcal BP). *Radiocarbon* In press.
2. P. J. Reimer *et al.*, IntCal13 and marine13 radiocarbon age calibration curves 0-50,000 years cal BP. *Radiocarbon* **55**, 1869–1887 (2013).
3. H. Oeschger *et al.*, ^{14}C and other parameters during the Younger Dryas cold phase. *Radiocarbon* **22**, 299–310 (1980).
4. T. Goslar *et al.*, High concentration of atmospheric ^{14}C during the Younger Dryas cold episode. *Nature* **377**, 414–417 (1995).
5. K. A. Hughen *et al.*, Deglacial changes in ocean circulation from an extended radiocarbon calibration. *Nature* **391**, 65–68 (1998).
6. C. Laj, H. Guillou, C. Kissel, Dynamics of the earth magnetic field in the 10-75 kyr period comprising the Laschamp and Mono Lake excursions: New results from the French Chaîne des Puys in a global perspective. *Earth Planet. Sci. Lett.* **387**, 184–197 (2014).
7. R. Muscheler, J. Beer, P. W. Kubik, H. A. Synal, Geomagnetic field intensity during the last 60,000 years based on ^{10}Be and ^{36}Cl from the Summit ice cores and ^{14}C. *Quat. Sci. Rev.* **24**, 1849–1860 (2005).
8. E. Bard, Geochemical and geophysical implications of the radiocarbon calibration. *Geochim. Cosmochim. Acta* **62**, 2025–2038 (1998).
9. K. Hughen *et al.*, ^{14}C activity and global carbon cycle changes over the past 50,000 years. *Science* **303**, 202–207 (2004).
10. H. Cheng *et al.*, Atmospheric ^{14}C/^{12}C changes during the last glacial period from Hulu Cave. *Science* **362**, 1293–1297 (2018).
11. E. Bard, F. Rostek, G. Ménot-Combes, Radiocarbon calibration beyond 20,000 B.P. by means of planktonic foraminifera of the Iberian Margin. *Quat. Res.* **61**, 204–214 (2004).
12. C. S. M. Turney *et al.*, The potential of New Zealand kauri (Agathis australis) for testing the synchronicity of abrupt climate change during the Last Glacial Interval (60,000-11,700 years ago). *Quat. Sci. Rev.* **29**, 3677–3682 (2010).
13. T. J. Heaton *et al.*, The IntCal20 approach to radiocarbon calibration curve construction: A new implementation using Bayesian splines and errors-in-variables. *Radiocarbon* In press.
14. J. F. O'Connell *et al.*, When did *Homo sapiens* first reach Southeast Asia and Sahul? *Proc. Natl. Acad. Sci. U.S.A.* **115**, 8482–8490 (2018).
15. Q. Fu *et al.*, A revised timescale for human evolution based on ancient mitochondrial genomes. *Curr. Biol.* **23**, 553–559 (2013).
16. C. Bronk Ramsey, Bayesian analysis of radiocarbon dates. *Radiocarbon* **51**, 337–360 (2009).

Dataset S1: Radiocarbon and calendar ages of Neanderthals and *Homo sapiens* used in Fig.2

	Neanderthals	AMS lab Code	^{14}C age	1 sig error	Cal BP with IntCal13				Cal BP with IntCal20			
					from	to	mean	1 sig error	from	to	mean	1 sig error
1	Les Rochers-de-Villeneuve, France	OxA-15257	45200	1100	49670	47640	48390	940	48670	46210	47910	1430
2	Saint-Césaire, France	OxA-18099	36200	750	41550	40110	40780	710	41860	40690	41160	580
3	Arcy-sur-Cure, France	MAMS-25149	36840	660	41980	40840	41350	570	42080	41270	41620	410
4	Les Cottés, France	MAMS-26196	39485	271	43410	42920	43210	250	42970	42680	42850	160
5	Spy 737a, Belgium	OxA-10560	36250	500	41400	40380	40860	490	41750	40930	41280	400
6	Goyey (1) Q53-4, Belgium	GrA-54022	39870	400	43900	43130	43570	380	43750	42720	43220	380
7	Goyey (2) Q55-1, Belgium	GrA-54257	37890	350	42420	41920	42170	250	42370	42090	42230	140
8	Goyey (3) Q56-1, Belgium	GrA-46170	38440	340	42740	42260	42510	240	42560	42280	42430	140
9	Goyey (4) Q57-1, Belgium	GrA-46173	41200	500	45170	44250	44700	460	44620	43440	44090	450
10	Goyey (5) Q305-4, Belgium	GrA-46176	40690	480	44710	43760	44250	460	44180	43270	43740	410
11	Goyey (6) Q376-1, Belgium	GrA-46178	39140	390	43240	42650	42990	310	42860	42510	42720	200
12	Neander Valley (1) NN4, Germany	ETH-19661	40360	760	44620	43280	44050	660	44110	42970	43630	550
13	Neander Valley (2) Nean 1, Germany	ETH-20981	39900	620	44130	43040	43660	540	43850	42730	43350	480
14	Neander Valley (3) NN1, Germany	ETH-19660	39240	670	43610	42540	43190	550	43150	42390	42960	470
15	Vindija Cave, Vi-33.26, Croatia	OxA-V-2291-18	44450	550	48430	47010	47790	700	47320	46080	46840	610
	Homo sapiens											
16	Ust'-Ishim, Siberia	OxA= weighted mean	41410	960	45770	44010	45010	930	44970	43340	44380	820
17	Pestera cu Oase, Romania	OxA+GrA= weighted mean	34950	990	40670	38520	39580	1090	41180	39190	39980	1050
18	Bacho Kiro (1), Bulgaria	ETH-86772	42450	510	46190	45250	45780	490	45430	44640	45120	400
19	Bacho Kiro (2), Bulgaria	ETH-86770	41850	480	45660	44800	45250	430	45010	44320	44690	380
20	Bacho Kiro (3), Bulgaria	ETH-86771	40600	420	44580	43720	44160	420	44080	43240	43690	380
21	Bacho Kiro (4), Bulgaria	ETH-86769	39750	380	43760	43050	43470	360	43240	42700	43110	350
22	Tianyuan Cave, China	BA-03222	34430	510	39560	38450	39000	600	40330	39130	39560	660

	References
1	Beauval, C., F. Lacrampe-Cuyaubère, B. Maureille and E. Trinkaus. "Direct radiocarbon dating and stable isotopes of the Neandertal femur from Les Rochers-de-Villeneuve (Lussac-les-Châteaux, Vienne)." *Bulletins et Memoires de la Societe d'Anthropologie de Paris* 18 (1-2): 35-42, (2006).
2	Hublin, J.-J., S. Talamo, M. Julien, F. David, N. Connet, P. Bodu, B. Vandermeersch and M. P. Richards. Radiocarbon dates from the Grotte du Renne and Saint-Césaire support a Neandertal origin for the Châtelperronian. *Proceedings of the National Academy of Sciences* 109(46): 18743-18748, (2012).
3	Welker, F., M. Hajdinjak, S. Talamo, K. Jaouen, M. Dannemann, F. David, M. Julien, M. Meyer, J. Kelso, I. Barnes, S. Brace, P. Kamminga, R. Fischer, B. M. Kessler, J. R. Stewart, S. Pääbo, M. J. Collins and J.-J. Hublin. Palaeoproteomic evidence identifies archaic hominins associated with the Châtelperronian at the Grotte du Renne. *Proceedings of the National Academy of Sciences* 113(40): 11162-11167, (2016).
4	Jaouen, K., M. Beasley, M. Schoeninger, J.-J. Hublin and M. P. Richards. Zinc isotope ratios of bones and teeth as new dietary indicators: results from a modern food web (Koobi Fora, Kenya). *Scientific Reports* 6: 26281, (2016).
5	Toussaint, M. and S. Pirson. Neandertal studies in Belgium: 2000–2005. *Periodicum Biologorum* 108(3): 373-387, (2006).
6	Rougier, H., I. Crevecoeur, C. Beauval, C. Posth, D. Flas, C. Wißing, A. Furtwängler, M. Germonpré, A. Gómez-Olivencia, P. Semal, J. van der Plicht, H. Bocherens and J. Krause. Neandertal cannibalism and Neandertal bones used as tools in Northern Europe. *Scientific Reports* 6: 29005, (2016).
7	Rougier, H., et al. (2016)
8	Rougier, H., et al. (2016)
9	Rougier, H., et al. (2016)
10	Rougier, H., et al. (2016)
11	Rougier, H., et al. (2016)
12	Schmitz, R.W., D. Serre, G. Bonani, S. Feine, F. Hillgruber, H. Krainitzki, S. Pääbo and F. H. Smith. The Neandertal type site revisited: Interdisciplinary investigations of skeletal remains from the Neander Valley, Germany. *Proceedings of the National Academy of Sciences* 99(20): 13342-13347, (2002).
13	Schmitz, R.W., et al. (2002)
14	Schmitz, R.W., et al. (2002)
15	Green, R. E., et al. A Draft Sequence of the Neandertal Genome. *Science* 328: 710-722, (2010).
16	Fu, Q., H. Li, P. Moorjani, F. Jay, S. M. Slepchenko, A. A. Bondarev, P. L. F. Johnson, A. Aximu-Petri, K. Prufer, C. de Filippo, M. Meyer, N. Zwyns, D. C. Salazar-Garcia, Y. V. Kuzmin, S. G. Keates, P. A. Kosintsev, D. I. Razhev, M. P. Richards, N. V. Peristov, M. Lachmann, K. Douka, T. F. G. Higham, M. Slatkin, J.-J. Hublin, D. Reich, J. Kelso, T. B. Viola and S. Pääbo. Genome sequence of a 45,000-year-old modern human from western Siberia. *Nature* 514(7523): 445-449, (2014).
17	Trinkaus, E., O. Moldovan, S. Milota, A. Bîlgar, L. Sarcina, S. Athreya, S. E. Bailey, R. Rodrigo, G. Mircea, T. Higham, C. B. Ramsey and J. v. d. Plicht. An early modern human from the Pestera cu Oase, Romania. *Proceedings of the National Academy of Sciences* 100(20): 11231-11236, (2003).
18	Hublin, J.-J., N. Sirakov, V. Aldeias, S. Bailey, E. Bard, V. Delvigne, E. Endarova, Y. Fagault, H. Fewlass, M. Hajdinjak, B. Kromer, I. Krumov, J. Marreiros, N. L. Martisius, L. Paskulin, V. Sinet-Mathiot, M. Meyer, S. Pääbo, V. Popov, Z. Rezek, S. Sirakova, M. M. Skinner, G. M. Smith, R. Spasov, S. Talamo, T. Tuna, L. Wacker, F. Welker, A. Wilcke, N. Zahariev, S. P. McPherron and T. Tsanova. Initial Upper Palaeolithic Homo sapiens from Bacho Kiro Cave, Bulgaria. *Nature* 581(7808): 299-302, (2020).
19	Fewlass, H., S. Talamo, L. Wacker, B. Kromer, T. Tuna, Y. Fagault, E. Bard, S. P. McPherron, V. Aldeias, R. Maria, N. L. Martisius, L. Paskulin, Z. Rezek, V. Sinet-Mathiot, S. Sirakova, G. M. Smith, R. Spasov, F. Welker, N. Sirakov, T. Tsanova and J.-J. Hublin (2020). "A 14C chronology for the Middle to Upper Palaeolithic transition at Bacho Kiro Cave, Bulgaria." Nature Ecology & Evolution 4, 794-801, (2020)
20	Hublin et al. (2020), Fewlass et al. (2020)
21	Hublin et al. (2020), Fewlass et al. (2020)
22	Hublin et al. (2020), Fewlass et al. (2020)
	Shang, H., H. Tong, S. Zhang, F. Chen and E. Trinkaus. An early modern human from Tianyuan Cave, Zhoukoudian, China. *Proceedings of the National Academy of Sciences* 104(16): 6573, (2007).